iScience

CellPress
OPEN ACCESS

Article

Bubble DNA tweezer: A triple-conformation sensor responsive to concentration-ratios

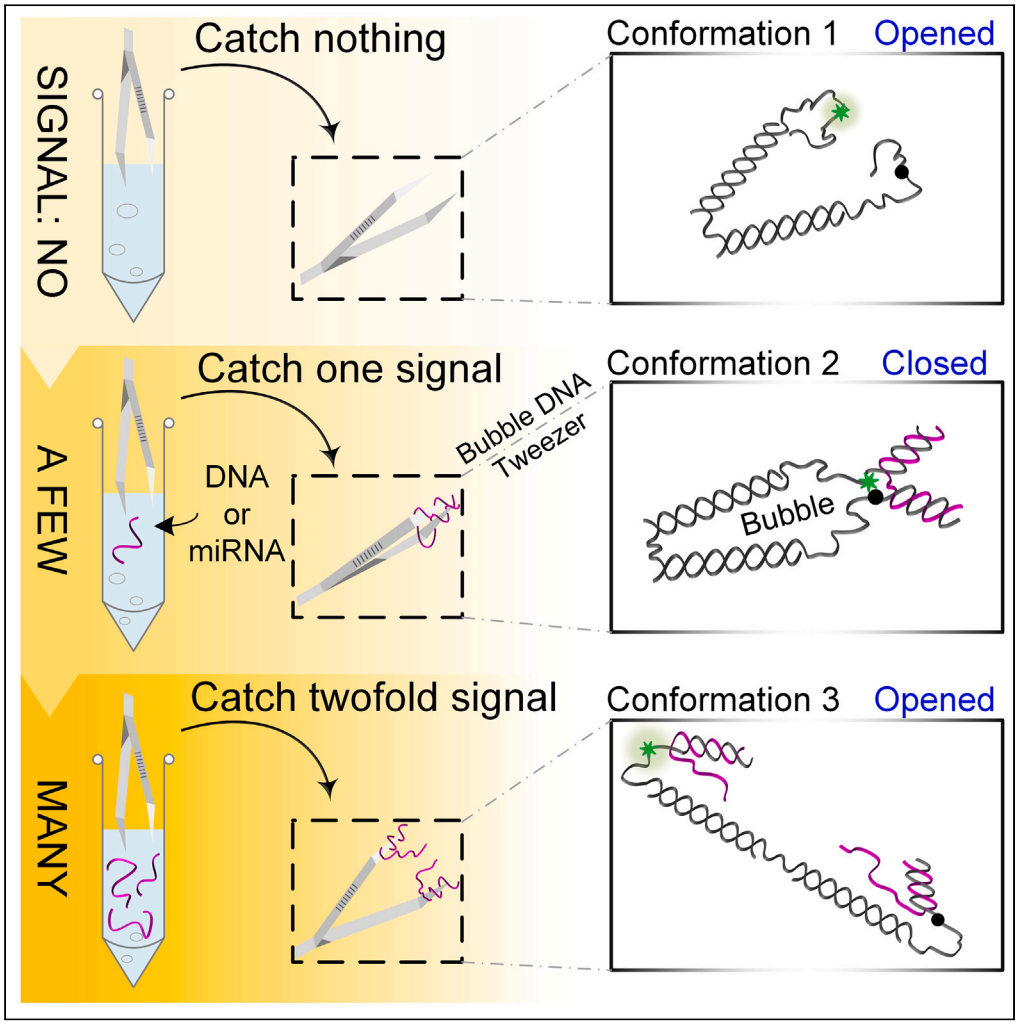

Yao Yao, Yuan Liu, Xin Liu, ..., Xiaokang Zhang, Qiang Zhang, Xiaopeng Wei

zhangq@dlut.edu.cn

Highlights

The bubble DNA tweezer can detect presence/absence and quantify the target signals

Triple-conformation is altered by target signal ratios

Unconventional rigid structure—highly flexible and loose structural features

Yao et al., iScience 27, 109074
March 15, 2024
https://doi.org/10.1016/j.isci.2024.109074

iScience

CellPress
OPEN ACCESS

Article

Bubble DNA tweezer: A triple-conformation sensor responsive to concentration-ratios

Yao Yao,[1] Yuan Liu,[1] Xin Liu,[1] Xun Zhang,[1] Peijun Shi,[1] Xiaokang Zhang,[1] Qiang Zhang,[1,2,*] and Xiaopeng Wei[1]

SUMMARY

DNA tweezers, with their elegant simplicity and flexibility, have been pivotal in biosensing and DNA computing. However, conventional tweezers are confined to a binary transformation pre/post target signal recognition, limiting them to presence/absence judgments. This study introduces bubble DNA tweezers (BDT), capable of three distinct conformations based on variable target signal ratios. In contrast to traditional compact tweezers, BDT features a looser structure centered around a non-complementary bubble domain located between the tweezer arms' connecting axis and target signal recognition jaws. This bubble triggers toehold-free DNA strand displacement, leading to three conformational changes at different target signal concentrations. BDT detects presence/absence and true concentration with remarkable specificity and sensitivity. This adaptability is not confined to ideal scenarios, proving valuable in complex, noisy environments. Our method facilitates target DNA/miRNA signal quantification within a specific length range, promising applications in clinical research and environmental detection, while inspiring future biological assay innovations.

INTRODUCTION

Since its inception, DNA computing[1] has rapidly advanced owing to its specificity and programmability. The introduction of multifunctional DNA structures, including nano-cages,[2] gears,[3] walkers,[4] and tweezers,[5] has enabled breakthroughs in molecular circuits,[6] nanomachines,[7] and molecular signal detection.[8,9] Among these, the DNA tweezer structure[10] stands out owing to its flexible opening and closing dynamics. As the name suggests, DNA tweezers resemble the shape of regular tweezers. Typically, these tweezers comprise a rigid, double-stranded DNA structure forming the fundamental clamp arms. They operate by controlling DNA hybridization to identify and manipulate target molecules. Guided by a flexible connecting axis, the double arms can adjust their position, mimicking the grasping action of surgical forceps on the target. The distinctiveness of DNA tweezers lies in their reversible conformational changes, enabling them to capture and release targets. Consequently, they hold promise as components in molecular switches,[11] biosensing,[12] and medical diagnostics,[13] driving extensive research efforts in these fields.

This dynamic changes in the geometric shape of the DNA tweezers, giving rise to distinctive signaling outcomes.[14] Meticulously designing the lengths of different connecting axis domains within DNA tweezers allows for precise spatial tuning.[15,16] Consequently, the DNA within the tweezers' jaw region can be engineered to dynamically sense environmental changes, generating corresponding signal outputs that enable swift detection of target substances.[17] DNA tweezers thus possess structural flexibility, enabling modulation of their spatial dimensions and demonstrating robust versatility and scalability. Researchers have leveraged these attributes to create varied nano-devices for identifying biological macromolecules like DNA and miRNA, opening innovative avenues for biosensing and molecular circuit advancements. In DNA detection, researchers employ a signal amplification strategy driven by an autocatalytic mechanism and design tweezers that can sensitively detect DNA in low-abundance environments, while possessing renewable and precise regulatory properties.[18] Furthermore, scientists have developed unlabeled and highly sensitive DNA sensors utilizing three strands. These sensors incorporate a G-quadruplex structure to enable fluorescence expression.[19] Leveraging the concept of activating DNA tweezers through proximity-based connectivity analysis, researchers have realized an innovative one-step amplification fluorescence detection method for DNA, successfully analyzing DNA in human serum.[20] Concerning miRNA detection, miRNA, originating from cellular expression, can also serve as markers for a variety of diseases. Given the significant impact of miRNA on disease progression and recovery, concentrations of miRNA have attracted substantial attention for their potential role in early diagnosis and subsequent treatment strategies.[21] Researchers have devised an unlabeled tweezer based on DNA double crossover. When a target miRNA is detected, this tweezer transforms the guanine-rich sequence on its arm into a G-quadruplex structure, thereby enabling signal expression.[22,23] This design offers the advantages of cost-effectiveness and enhanced sensitivity. In addition to planar DNA tweezers, 3D counterparts, often adopting tetrahedral structures, are also employed. While the receptor miRNA is absent, the tweezers remain relaxed; however, the presence of the target receptor prompts a tightening response, leading to observable fluctuations in the

[1]School of Computer Science and Technology, Dalian University of Technology, Dalian, Liaoning 116024, China
[2]Lead contact
*Correspondence: zhangq@dlut.edu.cn
https://doi.org/10.1016/j.isci.2024.109074

fluorescence intensity.[24,25] Differently from their 2D counterparts, 3D tweezers possess larger geometric dimensions, enabling more significant changes in fluorescence intensity. Beyond DNA and miRNA, tweezers find broad utility in the detection of hormones,[13] adenosine,[26,27] pH,[28] toxins[29,30] and heavy metal ions.[31]

However, in the past, DNA-tweezer-based tools used for biological signal detection were often limited to determining only the presence or absence of a signal, essentially yielding binary outcomes of 1 or 0.[10] This limitation arises from the fact that their tweezers can only undergo two conformational transitions, one before and one after picking up the target signal, making it difficult to measure the strength of the signal. For DNA and miRNA signals, their "concentration" in the liquid phase environment represents their "signal strength". For ease of expression on the context, we will use suitable terminology throughout this article. To address this limitation, we embarked on an in-depth exploration of the structure of DNA tweezers, leading us to an intriguing discovery. When a tweezer with a bubble structure reaches a specific threshold proportional to the target signal, it exhibits an "abnormal" structural change, which is confirmed by the significantly changed fluorescence curve and gel electrophoresis. This phenomenon immediately captured our attention, prompting us to conduct detailed research. It was during this investigation that we unveiled the concept of bubble DNA tweezers (BDT) driven by toehold-free DNA strand displacement (TFDSD). BDT exhibits three conformations: conformation 1 when no target signal is present; conformation 2 when there is a target signal and its concentration does not exceed that of BDT; and conformation 3 when the concentration of the target signal exceeds that of BDT. Experimental findings showcase that this feature of BDT not only allows for binary determination of the presence (1) or absence (0) of the target signal, but also enables quantification of the target signal's true intensity using fluorescence inflection points in subsequent titration modes. Therefore, BDT could present a fresh method or sensor prototype for medical diagnosis and environment detection. Sensors with this characteristic may drive the paradigm shift of biosensing from binary results to accurate values.

RESULTS

Mechanism of bubble DNA tweezer

Figure 1A illustrates the fundamental scheme of the BDT. According to the different ratios of BDT to target signals, BDT exhibits three different conformations: C_1, C_2 and C_3. C_1 is the opened (original) state, C_2 is the closed state, and C_3 is the reopened state. The S represents the target signal. In contrast to traditional DNA tweezers,[10] BDT exhibits two significant differences: 1. BDT has the capability to transform two different structures based on varying ratios with the target signal, a versatility not present in traditional tweezers, which can only undergo one structural change for a single target signal; 2. The main body of BDT includes a lengthy single-chain, non-complementary bubble region, endowing BDT with a highly flexible and loose structure. However, traditional tweezers feature a rigid and compact structure composed of double chains.

Figure 1B specifically describes the biochemical process of this mechanism. Comprising three uncomplicated DNA single strands (annealing process in Figure S1), the P3 strand functions as the connecting axis, while the a* and d* segments extend to a length of 18 nt for enhanced stability. The g domain, comprising 4 Thymine, ensures BDT's structural flexibility. The P1 and P2 strands function as clamp arms, with the c and f domains serving as jaws for target signal recognition. The length and sequence of these components are tailored to the specific target signal. The b and e domains constitute the bubble, spanning 18 nt and designing as mismatched sequences. The connection between the bubble and jaw on both clamp arms is labeled with FAM fluorescence and BHQ1 quenching labels. The designed target signal S is partitioned into two signal domains, c* and f*, with equal base numbers. These signal domains complement the two jaw domains c and f of BDT, respectively. In the absence of S input, BDT appears in an open state (C_1, composed of three DNA strands). At this time, the FAM is distant from BHQ1, resulting in high fluorescence intensity. With a small S amount, the first-stage reaction occurs, forming a double-stranded structure with the two jaws (C_2, composed of four DNA strands). This shortens the distance between FAM and BHQ1 and causing a decrease in fluorescence. With a large S amount (S to BDT ratio exceeding 1:1), the second-stage reaction occurs. Excessive S invades the closed structure of C_2 through the bubble domain, initiating a TFDSD reaction. In this phase, each jaw domain of BDT combines with one signal domain of S to form a double strand. Simultaneously, each S retains a free, unpaired signal domain that cannot form a double strand. The closed structure reopens (C_3, composed of five DNA strands), increasing the distance between FAM and BHQ1 and causing a rise in fluorescence intensity.

The experimental results firmly validate the previously outlined attributes of BDT. As illustrated in Figure 2A, the C_1-C_2-C_3 transition involves a large-small-large distance change between FAM and BHQ1, manifesting as a high-low-high V-shaped fluorescence trajectory. In the C_1 state, there is an excessively long single-chain DNA structure. Governed by the worm-like chain model,[32] the segment (bubble and jaw) containing FAM and BHQ1 curls up at both ends of the rigid connecting axis domain. As the system transitions to the C_3 state, the single-chain structure decreases, weakening the curling effect. Meanwhile, under the action of 2×S, the distance between the BDT clamp arms is further stretched. Consequently, the distance between FAM and BHQ1 becomes slightly greater than that in the C_1 state. Therefore, the fluorescence in the C_3 state may be higher than that in the C_1 state. In addition, we have conducted tests at higher temperatures and still exhibit V-shaped fluorescence characteristics (Figure S2). In Figure 2B, after experiencing the same reaction time as Figure 2A, electrophoresis was performed. S gradually increases in increments of 0.5 times, and the position of the bands indicates the alternating appearance and gradual disappearance of the C_1, C_2, and C_3 conformations. Both fluorescence and electrophoresis phenomena indicate that BDT can accurately perceive the moment when the ratio to the target signal S is 1:1, which provides the possibility of using BDT to measure the concentration of the target signal. Yet, the potential of BDT goes beyond that. It seamlessly integrates into the realm of DNA computing and molecule circuits, bringing together two essential components—a switch and a reporter. Interestingly, this logic switch exhibits a special breakdown characteristic, as depicted in Figures S3 and S4.

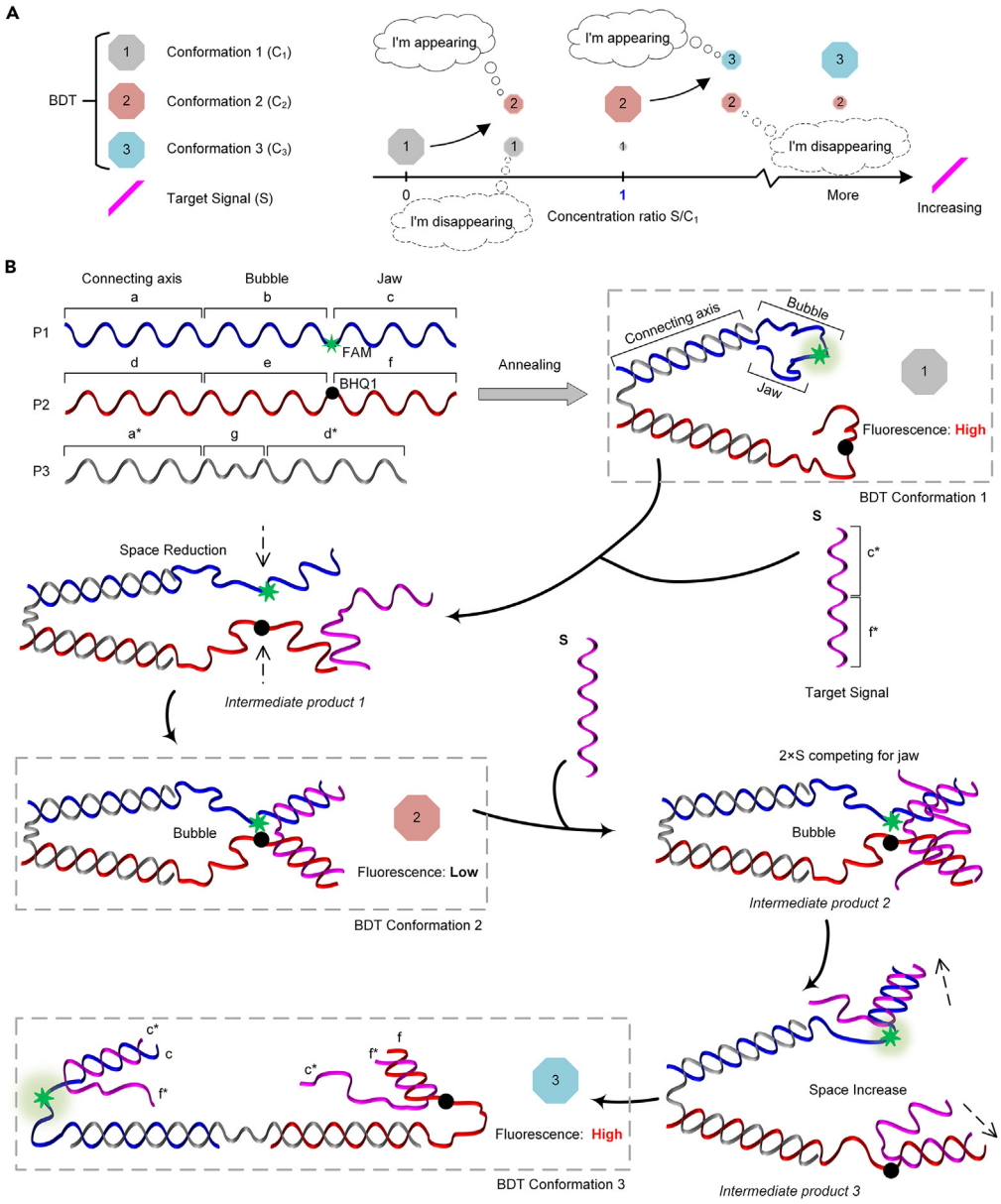

Figure 1. BDT scheme

(A) Overview of BDT triple conformational transformation: as S increases, C_2 and C_3 appear sequentially, while C_1 and C_2 gradually disappear.

(B) The biological mechanism underlying the formation of distinct conformations resulting from the interaction between BDT and varying proportions of S.

The BDT scheme undergoes multiple conformational changes in response to the target signal concentration, representing a significant departure from conventional approaches. It unequivocally charts a new course in the exploration of DNA configurations and strand displacement. Our BDT design transitions through three distinctive conformations across varying target signal concentration ratios, resulting in significant fluorescence changes during these transformations. This not only facilitates the determination of target signal presence (1) or absence (0) but also empowers the measurement of target signal intensity based on the initial BDT concentration. This breakthrough effectively dismantles the inherent constraints of traditional dual-conformation DNA tweezers.

Jaw length dependency in BDT structure

The range of achievable target signal measurements is determined by the jaw length of BDT. To investigate this range, we conducted gradient experiments by varying the length of the target signal. The results of these experiments are illustrated in Figure 3. In these trials, we subjected the conformation C_1 to a 1:1 ratio reaction with the target signal A. Figure 3A delineates two distinct scenarios of target signal

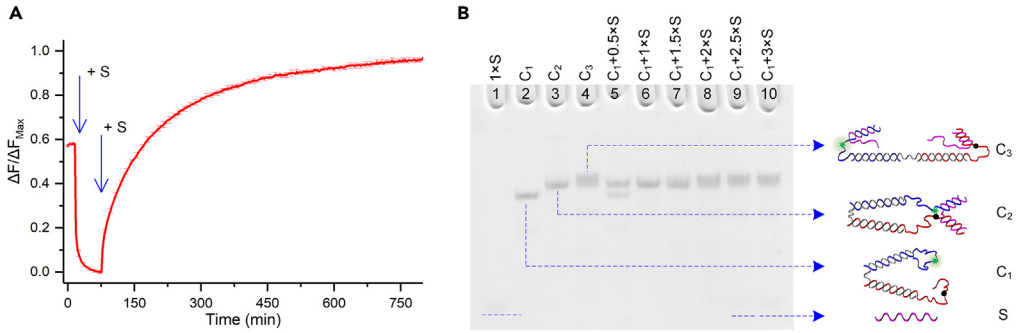

Figure 2. Fluorescence and electrophoretic characteristics of BDT

(A) The fluorescence changes after adding 1×S twice to C_1. Here, 1× is defined as the concentration of a species in a solution (the same below, unless otherwise specified). In this context, 1× represents a concentration of 1 μM, and the concentration in solution $[C_1] = 1×$. Here, ΔF represents the increment of the current fluorescence value relative to the lowest, ΔF_{Max} represents the biggest ΔF in entire reaction process.

(B) Electrophoretic results of BDT at different ratios of S. The substances in different swimming lanes: lane 1 1×S, lane 2 C_1, lane 3 C_2, lane 4 C_3, lane 5 C_1+0.5×S, lane 6 C_1+1×S, lane 7 C_1+1.5×S, lane 8 C_1+2×S, lane 9 C_1+2.5×S, lane 10 C_1+3×S. In lanes 2–10, all BDTs are at 1× concentration (C_1, C_2 or C_3).

A, each with varying lengths. Notably, when A was sufficiently long, C_1 adeptly transitioned from an open to a closed state (C_2), attesting to BDT's robust recognition capability for long target signals. Conversely, when A fell short in length, the insufficient binding capacity of the bases inhibited C_1 from achieving complete closure. Instead, this circumstance prompted further opening of the tweezers.

The real-time fluorescence observations presented in Figure 3B further clarify this principle. The target signal A was symmetrically partitioned into two segments of equal length, and a gradient assessment was conducted, ranging from 20 nt to 6 nt on a single side. The experimental findings indicate that when the unilateral length was equal to or greater than 12 nt, BDT achieved an optimal closure state, signifying BDT's robust capability in detecting longer target signals. However, when the unilateral length reached 10 nt, BDT began to exhibit incomplete closure, yet still demonstrates a significant reduction in fluorescence. As the unilateral length continued to decrease, BDT became unable to achieve full closure, signifying the loss of its capacity to detect shorter target signals.

In addition to the length of the target signal influencing the reaction kinetics, the GC content in the target signal may also have an impact. Generally, higher GC content accelerates the hybridization reaction,[33] but it also increases the probability of complex structures emerging, such as hairpins, G-quadruplexes, or i-motifs.[34,35] Therefore, predicting the impact of variations in GC content in the target signal on reaction kinetics is highly complex in practical scenarios. Furthermore, experimentally confirming this issue is also challenging. For instance, sequences with the same GC content but varying arrangements of G and C in the sequence, may lead to different complex structures.

Bubble scale dependency in BDT structure

The bubble scale underpins BDT's capability for a TFDSD reaction. To assess the influence of the mismatched bubble scale on BDT's characteristics, we conducted a gradient study with bubbles ranging from 18 nt to 1 nt, as depicted in Figure 4. Given the previously validated

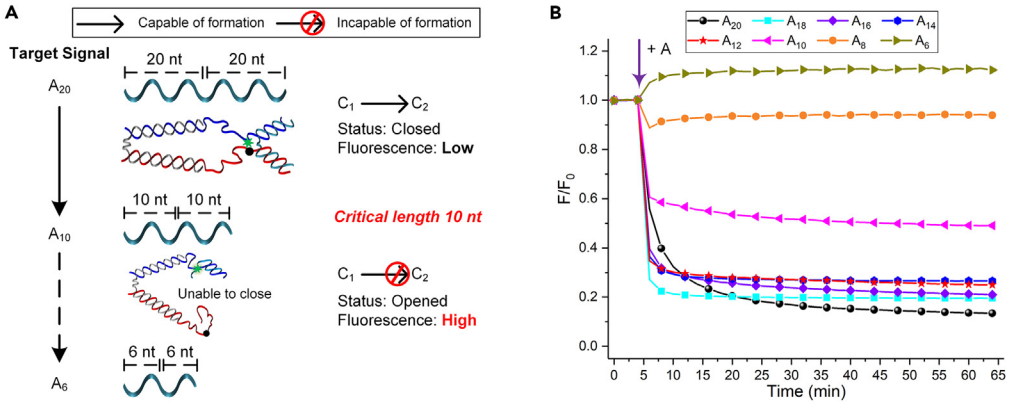

Figure 3. Analysis of jaw length gradient in BDT

(A) Research on the effect of changes in target signal length on BDT's recognition ability. When the length of the target signal is less than 20 nt, BDT may encounter challenges in achieving closure.

(B) Real time fluorescence results of target signal A with different lengths. Optimal fluorescence characteristics are achieved by BDT when the length of the target signal exceeds 24 nt. Here, F_0 represents the initial fluorescence value, while F represents the specific fluorescence value at each moment. $[C_1] = [A] = 1×$.

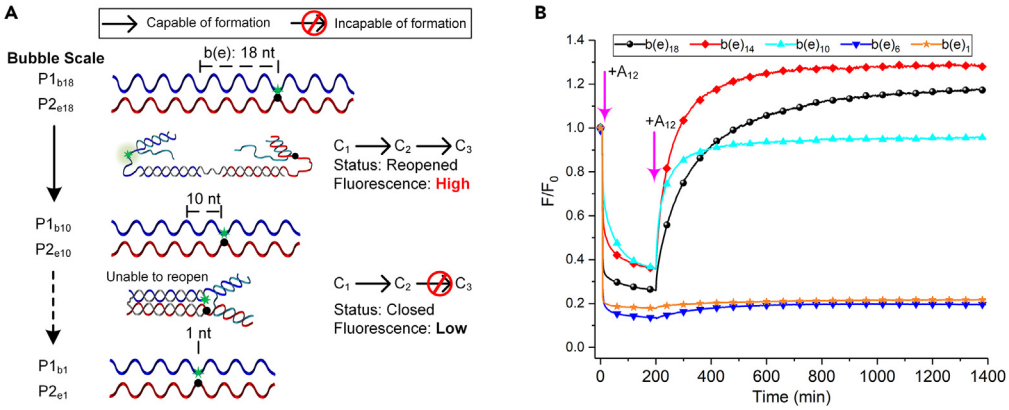

Figure 4. Analysis of bubble scale gradient in BDT

(A) Research on the effect of bubble scale change on the BDT V-shaped kinetics. When the bubble scale exceeds 10 nt, BDT is expected to undergo the complete process of C_1-C_2-C_3. In contrast, it cannot be reopened after reaching the closed state of C_2. The b(e) represents b domain and e domain.

(B) Real-time fluorescence results and the effect of bubble size changes on the maintenance of the BDT V-shaped characteristic. Bubbles below 10 nt, even when an excessive signal is added, do not exhibit fluorescence rebound. Here, F_0 represents the initial fluorescence value, while F represents the specific fluorescence value at each moment. [C_1] = 1×. Adding twice 1×A_{12}.

observation that a unilateral length of 12 nt or more in the target signal yielded the most favorable outcomes, we employed A_{12} with a unilateral length of 12 nt for this validation. Figure 4A illustrates the validation principle. We injected 1×A_{12} into C_1 twice. When the b and e domains within the bubbles were of substantial lengths, the tweezers achieved complete expansion, enabling the TFDSD reaction, and resulting for C_3. Conversely, in cases where the bubble field was diminutive, the tweezers remained tightly shut, rendering them incapable of reopening, and resulting only in C_2.

The fluorescence phenomenon depicted in Figure 4B provides further validation of this kinetic pattern. When b(e) reached or exceeded 10 nt, the distinct V-shaped fluorescence kinetics could be observed. However, various bubble lengths exerted a certain influence on the tweezers' opening rate and reaction extent. As the b(e) length was further reduced, the characteristic V-shaped fluorescence kinetics became less pronounced. Consequently, this experiment not only elucidated the influence of bubbles on tweezers' behavior but also revealed the requisite bubble dimensions.

In summary, the results of the two conducted experiments—involving the exploration of jaw length and the analysis of bubble size—unequivocally demonstrate that BDT could detect target signals of 20 nt and beyond. Conversely, its recognition ability was limited for signals of shorter length. Furthermore, an optimal bubble size seemed to fall within the range of 14 nt–18 nt. Overly small bubble sizes could lead to the loss of characteristic V-shaped fluorescence kinetics.

The BDT limit of detection for biosensing

BDT is well-suited for measuring the length of the target signal, aligning with the typical range of miRNA lengths, which is 20 nt–24 nt. The V-shaped fluorescence performance of target signal lengths ranging from 12 nt to 40 nt is demonstrated in Figure S5. The increasing significance of miRNA in disease diagnosis and treatment underscores its vast medical potential. Leveraging the high specificity and biocompatibility of DNA, researchers have recently engaged in more collaborative research at the intersection of these two areas.[23,36,37]

To evaluate the detection sensitivity and linear range of the BDT strategy, we proceeded by analyzing the limit of detection (LOD) using A_{12} as the target signal. In Figure 5A, FAM was used as a fluorescent label with a maximum emission around the 518 nm wavelength. This concentration sensitivity experimentation ranged from 0.01 nM to 50 nM.

The linear regression process in Figure 5B, with the concentration of A_{12} on the horizontal axis, showcases the robust linear response of BDT, boasting a remarkable coefficient of determination (R^2) of 0.98937. Employing the calculation formula LOD = 3σ/S (where σ represents the standard deviation of fluorescence intensity across 11 blank input samples, and S signifies the slope of the regression line), the LOD is evaluated to be 9 pM. This outcome attests to BDT's sensitivity. BDT is a linear system with slightly lower sensitivity than nonlinear systems (e.g., logarithmic system).

Specificity and application of the BDT in miRNA measurement

Research findings have indicated the regulatory roles of miR-29b in skeletal muscle atrophy and the development of certain tumor cells.[38–40] Given that miR-29b spans 24 nucleotides, it is an ideal target signal for BDT. To affirm the specificity of BDT, we conducted experiments involving the introduction of miR-29b, miR-155, miR-21, and miR-144 (all sequences derived from the Library miRDB),[41] into separate test tubes at identical concentrations. To prevent any fluorescence rebound interference due to an overabundance of target signals, we kept the BDT:miRNA ratio at 1:0.9, as depicted in Figure 6A. The results from these experiments show that only miR-29b led to a pronounced reduction in fluorescence intensity, which is compelling evidence for the excellent selectivity of BDT toward miR-29b.

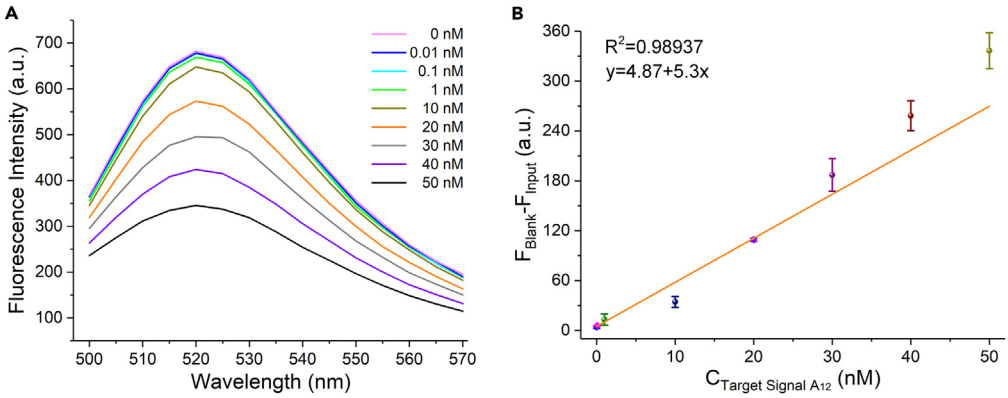

Figure 5. LOD analysis of BDT

(A) The effect of different concentrations of A_{12} on fluorescence intensity, from top to bottom, the $[A_{12}]$ are 0 nM, 0.01 nM, 0.1 nM, 1 nM, 10 nM, 20 nM, 30 nM, 40 nM and 50 nM. $[C_1]$ = 50 nM.

(B) Linear regression of the BDT on different concentrations range of target signal A_{12}. F_{Blank} represents the blank group ($[A_{12}]$ = 0 nM), while F_{Input} represents the specific fluorescence value at different $[A_{12}]$ (0.01 nM–50 nM), F_{Blank}-F_{Input} is the fluorescence variation.

Based on the significant changes in the V-shaped fluorescence trend at the inflection point, the titration method is reliable for measurement. Therefore, utilizing concentration variation relationships, we define the calculation Equation 1:

$$N_1V_tC_x/\Delta V < VC_{BDT}/\Delta V < N_2V_tC_x/\Delta V \quad \text{(Equation 1)}$$

where N_1 and N_2 represent titration times, with N_1 being the last titration prior to fluorescence rebound, and fluorescence rebounds following the completion of N_2 titration. C_x denotes the concentration of the substance to be measured. V stands for the initial volume of the BDT solution, while C_{BDT} represents its initial concentration (i.e., concentration of C_1). ΔV corresponds to the new volume of the solution after each titration, and V_t is the volume of each titration, which is a constant. The range of C_x can be determined using Equation 1, leading to Equation 2:

$$VC_{BDT}/N_2V_t < C_x < VC_{BDT}/N_1V_t \quad \text{(Equation 2)}$$

In Figure 6B, we verified the applicability of this method by mixing four different concentrations of miRNAs in a test tube (represented as Mix), with the other three serving as noise signals. The concentrations of the four components in the mixture were as follows: $C_{miR\text{-}29b}$ = 4 μM, $C_{miR\text{-}155}$ = 6 μM, $C_{miR\text{-}21}$ = 8 μM, and $C_{miR\text{-}144}$ = 10 μM. We set VC_{BDT} = 20 pmol, V_t = 0.8 μL, and observed fluorescence rebound phenomenon at N_1 = 6 and N_2 = 7. As a result, the range of C_x was determined to be between 3.57 μM and 4.17 μM, aligning with the concentration of miR-29b set in Mix. It is worth noting that using a smaller V_t leads to a more accurate measurement range. This experiment confirms that BDT can

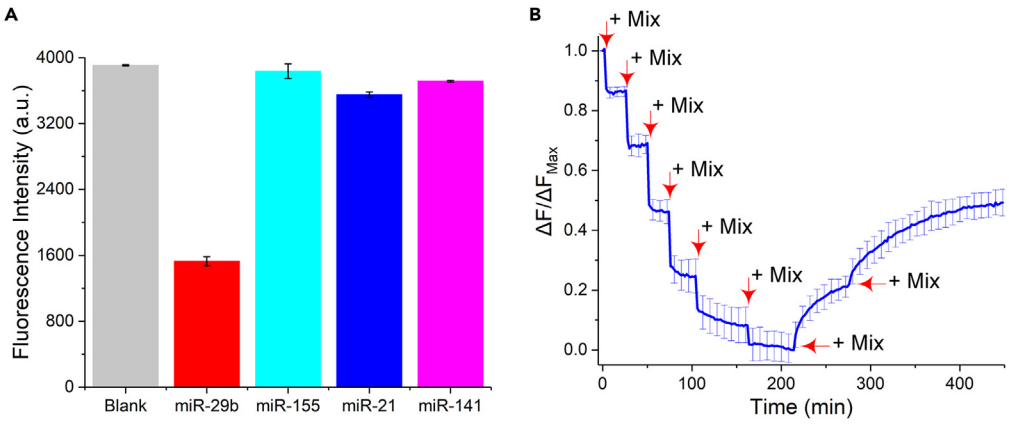

Figure 6. Specificity and application of the BDT in miRNA measurement

(A) Specificity of BDT, BDT:miRNA = 1:0.9. BDT is the conformation C_1, $[C_1]$ = 1×.

(B) The V-shaped fluorescence method of measuring the true strength of miR-29b using BDT ($[C_1]$ = 1×) in a multi-noise environment. Fluorescence rebound occurred during the 6th and 7th rounds of Mix titration. Here, ΔF represents the increment of the current fluorescence value relative to the lowest, ΔF_{Max} represents the biggest ΔF in entire reaction process.

not only detect the presence of target signals in noisy environments but also measure their intensity. In the example provided above, it's evident that within the first six titrations, the concentration of miR-29b (the solution under examination) in the system remains lower than that of BDT. This allows us to observe the distinctive V-shaped fluorescence and conduct subsequent calculations. However, in scenarios where the test solution's initial concentration surpasses that of BDT during the first titration, the observation of V-shaped fluorescence becomes challenging. In such cases, it becomes imperative to estimate and dilute the highly concentrated solution. Further details on this aspect are provided in Figure S6, and the concentration measurement algorithm is organized into Figure S7.

In Figure 6B, the DNA sequence corresponding to miR-29b is identical to the sequence of the target signal S illustrated in Figure 2. Although S represents DNA and miR-29b represents RNA, BDT exhibits the same fluorescence rebound effect for both, implying that the response of the BDT system is unaffected by the distinction between DNA and RNA.

DISCUSSION

This article introduces BDT, a DNA tweezer with three conformations, overcoming the binary (1/0) discrimination limitation of conventional tweezers. A crucial design element of BDT is the incorporation of a sufficiently large bubble domain. In the presence of this domain, the spatial configuration of the tweezers can be altered in response to the target signal ratio, generating a distinctive V-shaped fluorescence kinetics pattern. Quantification of the target signal occurs at the lowest point of the fluorescence curve. Notably, the synergy between BDT's specificity and sensitivity enables effective discrimination of target signals from a background of noise and measurement of a range of signal strengths. In sharp contrast to prevailing methodologies, where DNA tweezers merely confirm signal presence or absence,[10] BDT is a scheme capable of accurately determining the true intensity range of target signals through significant fluorescence changes.

Conceptually, our BDT has the potential to evolve from a single-jaw, three-state configuration to a more intricate setup with multiple jaws, allowing for comprehensive multi-signal measurements. However, some issues need to be addressed. First, the BDT requires a target signal length of at least 20 nt to yield meaningful outcomes. Consequently, addressing the detection of shorter target signals is necessary. Incorporating auxiliary DNA within the bubble (Figures S8–S10) presents a potential solution to enhance the capture capability for shorter target signals. Second, the design of bubbles demands meticulous attention to base mismatch considerations. Various mismatch combinations yield distinct impacts on the reaction rate and efficiency (Figure S11). As the BDT is expanded to encompass multiple jaws, the requirement for diverse bubble arrangements necessitates the design of numerous mismatched base configurations. Crafting these sequences poses a significant challenge. Currently, a viable approach involves initial non-complementary DNA screening through combinatorial optimization and evolutionary algorithms,[42,43] followed by real-time fluorescence validation.

In conclusion, BDT excels in differentiating and quantifying the strength of target signals, whether in simple scenarios involving single target signals or in complex environments with various background interferences. BDT could be applied to different areas, especially in applications with specific recognition needs or concentration concerns, such as medical diagnosis, targeted drug delivery, dynamic monitoring, environmental detection, etc. BDT is expected to become a sensor prototype and make potential contributions to these fields.

Limitations of the study

There are several notable limitations to our study. Although BDT demonstrates the capability to recognize and detect DNA/miRNA target signals over a broad range of lengths, it may not be well-suited for excessively long or too short signals. Furthermore, while BDT theoretically offers accurate quantification of target signal concentrations, practical implementation may be hindered by manual handling and experimental errors. The resulting concentration range is subject to the precision of the minimum titration volume achievable during the operation, making it suitable for scenarios with less stringent accuracy requirements.

STAR★METHODS

Detailed methods are provided in the online version of this paper and include the following:

- KEY RESOURCES TABLE
- RESOURCE AVAILABILITY
  - Lead contact
  - Materials availability
  - Data and code availability
- METHOD DETAILS
  - Reagent preparation
  - Design of oligonucleotide sequences
  - Annealing process protocol
  - Polyacrylamide gel electrophoresis protocol
  - Fluorescence scan protocol
- QUANTIFICATION AND STATISTICAL ANALYSIS
  - Oligonucleotide information statistics
  - Fluorescence data statistics

SUPPLEMENTAL INFORMATION

Supplemental information can be found online at https://doi.org/10.1016/j.isci.2024.109074.

ACKNOWLEDGMENTS

This work is supported by 111 Project (No. D23006), the National Natural Science Foundation of China (Nos. 62272079, 61972266), Liaoning Revitalization Talents Program (No. XLYC2008017), Natural Science Foundation of Liaoning Province (Nos. 2021-MS-344, 2021-KF-11-03, 2022-KF-12-14), the Postgraduate Education Reform Project of Liaoning Province (No. LNYJG2022493), the Dalian Outstanding Young Science and Technology Talent Support Program (No. 2022RJ08).

AUTHOR CONTRIBUTIONS

Methodology, Investigation and Writing–Original Draft, Y.Y.; Data Curation, Y.L.; Formal Analysis, X.L. and X.Z.; Writing–Review and Editing, P.J.S. and X.K.Z.; Supervision, Funding Acquisition, Q.Z.; Conceptualization, X.P.W.

DECLARATION OF INTERESTS

The authors declare no competing interests.

Received: October 19, 2023
Revised: January 12, 2024
Accepted: January 26, 2024
Published: February 1, 2024

REFERENCES

1. Adleman, L.M. (1994). Molecular computation of solutions to combinatorial problems. Science *266*, 1021–1024. https://doi.org/10.1126/science.7973651.
2. Zhao, S., Zhang, S., Hu, H., Cheng, Y., Zou, K., Song, J., Deng, J., Li, L., Zhang, X.B., Ke, G., and Sun, J. (2023). Selective in situ analysis of mature microRNAs in extracellular vesicles using a DNA cage-based thermophoretic assay. Angew. Chem. Int. Ed. *62*, e202303121. https://doi.org/10.1002/anie.202303121.
3. Peil, A., Xin, L., Both, S., Shen, L., Ke, Y., Weiss, T., Zhan, P., and Liu, N. (2022). DNA assembly of modular components into a rotary nanodevice. ACS Nano *16*, 5284–5291. https://doi.org/10.1021/acsnano.1c10160.
4. Valero, J., and Famulok, M. (2020). Regeneration of burnt bridges on a DNA catenane walker. Angew. Chem. Int. Ed. *59*, 16366–16370. https://doi.org/10.1002/anie.202004447.
5. Saliba, D., Trinh, T., Lachance-Brais, C., Prinzen, A.L., Rizzuto, F.J., de Rochambeau, D., and Sleiman, H.F. (2021). Asymmetric patterning drives the folding of a tripodal DNA nanotweezer. Chem. Sci. *13*, 74–80. https://doi.org/10.1039/d1sc04793k.
6. Jung, J.K., Archuleta, C.M., Alam, K.K., and Lucks, J.B. (2022). Programming cell-free biosensors with DNA strand displacement circuits. Nat. Chem. Biol. *18*, 385–393. https://doi.org/10.1038/s41589-021-00962-9.
7. Li, H., Gao, J., Cao, L., Xie, X., Fan, J., Wang, H., Wang, H.H., and Nie, Z. (2021). A DNA molecular robot that autonomously walks on the cell membrane to drive cell motility. Angew. Chem. Int. Ed. *60*, 26087–26095. https://doi.org/10.1002/anie.202108210.
8. Lee, S., Godhulayyagari, S., Nguyen, S.T., Lu, J.K., Ebrahimi, S.B., and Samanta, D. (2022). Signal transduction strategies for analyte detection using DNA-based nanostructures. Angew. Chem. Int. Ed. *61*, e202202211. https://doi.org/10.1002/anie.202202211.
9. Zhu, Y., Wu, J., and Zhou, Q. (2023). Functional DNA sensors integrated with nucleic acid signal amplification strategies for non-nucleic acid targets detection. Biosens. Bioelectron. *230*, 115282. https://doi.org/10.1016/j.bios.2023.115282.
10. Zhang, R., Chen, R., Ma, Y., Liang, J., Ren, S., and Gao, Z. (2023). Application of DNA nanotweezers in biosensing: nanoarchitectonics and advanced challenges. Biosens. Bioelectron. *237*, 115445. https://doi.org/10.1016/j.bios.2023.115445.
11. Xiong, X., Xiao, M., Lai, W., Li, L., Fan, C., and Pei, H. (2021). Optochemical control of DNA-switching circuits for logic and probabilistic computation. Angew. Chem. Int. Ed. *60*, 3397–3401. https://doi.org/10.1002/anie.202013883.
12. Li, C.Y., Zheng, B., Li, J.T., Gao, J.L., Liu, Y.H., Pang, D.W., and Tang, H.W. (2021). Holographic optical tweezers and boosting upconversion luminescent resonance energy transfer combined clustered regularly interspaced short palindromic repeats (CRISPR)/Cas12a biosensors. ACS Nano *15*, 8142–8154. https://doi.org/10.1021/acsnano.0c09986.
13. Zhang, J., Chen, M., Peng, Y., Li, S., Han, D., Ren, S., Qin, K., Li, S., Han, T., Wang, Y., and Gao, Z. (2022). Exploring the performance of multi-channel tetrahedral nucleic acid tweezers platforms for efficient and sensitive biosensing. Chem. Eng. J. *448*, 137635. https://doi.org/10.1016/j.cej.2022.137635.
14. Yurke, B., Turberfield, A.J., Mills, A.P., Simmel, F.C., and Neumann, J.L. (2000). A DNA-fuelled molecular machine made of DNA. Nature *406*, 605–608. https://doi.org/10.1038/35020524.
15. Aleman-Garcia, M.A., Orbach, R., and Willner, I. (2014). Ion-responsive hemin-g-quadruplexes for switchable DNAzyme and enzyme functions. Chem-Eur. J. *20*, 5619–5624. https://doi.org/10.1002/chem.201304702.
16. Gong, X., Zhou, W., Li, D., Chai, Y., Xiang, Y., and Yuan, R. (2015). RNA-regulated molecular tweezers for sensitive fluorescent detection of microRNA from cancer cells. Biosens. Bioelectron. *71*, 98–102. https://doi.org/10.1016/j.bios.2015.04.003.
17. Yang, W., Shen, Y., Zhang, D., Li, C., Yuan, R., and Xu, W. (2019). Programmed dual-functional DNA tweezer for simultaneous and recognizable fluorescence detection of microRNA and protein. Anal. Chem. *91*, 7782–7789. https://doi.org/10.1021/acs.analchem.9b01266.
18. Kou, B., Chai, Y., Yuan, Y., and Yuan, R. (2018). Dynamical regulation of enzyme cascade amplification by a regenerated DNA nanotweezer for ultrasensitive electrochemical DNA detection. Anal. Chem. *90*, 10701–10706. https://doi.org/10.1021/acs.analchem.8b00477.
19. Guo, J., Feng, C., Liu, Z., Ye, B., Li, G., and Zou, L. (2021). A label-free electrochemical biosensor based on novel DNA nanotweezer coupled with G-quadruplex for sensitive DNA detection. Sensor. Actuat. B-Chem. *331*, 129437. https://doi.org/10.1016/j.snb.2021.129437.
20. Yun, W., Zhu, H., Wu, H., Zhuo, L., Wang, R., Ha, X., Wang, X., Zhang, J., Chen, H., and Yang, L. (2021). A "turn-on" and proximity ligation assay dependent DNA tweezer for one-step amplified fluorescent detection of DNA. Spectrochim. Acta A. *249*, 119292. https://doi.org/10.1016/j.saa.2020.119292.
21. Lee, J.C., Zhao, J.T., Clifton-Bligh, R.J., Gill, A., Gundara, J.S., Ip, J.C., Glover, A., Sywak, M.S., Delbridge, L.W., Robinson, B.G., and Sidhu, S.B. (2013). MicroRNA-222 and microRNA-146b are tissue and circulating biomarkers of recurrent papillary thyroid cancer. Cancer-Am. Cancer Soc. *119*, 4358–4365. https://doi.org/10.1002/cncr.28254.

22. Li, D., Cheng, W., Li, Y., Xu, Y., Li, X., Yin, Y., Ju, H., and Ding, S. (2016). Catalytic hairpin assembly actuated DNA nanotweezer for logic gate building and sensitive enzyme-free biosensing of microRNAs. Anal. Chem. *88*, 7500–7506. https://doi.org/10.1021/acs.analchem.5b04844.
23. Agahi, M., and Rahaie, M. (2022). A novel DNA tweezers-based nanobiosensor for multiple detections of circulating exosomal microRNAs in breast cancer. Anal. Biochem. *651*, 114697. https://doi.org/10.1016/j.ab.2022.114697.
24. He, L., Lu, D.Q., Liang, H., Xie, S., Luo, C., Hu, M., Xu, L., Zhang, X., and Tan, W. (2017). Fluorescence resonance energy transfer-based DNA tetrahedron nanotweezer for highly reliable detection of tumor-related mRNA in living cells. ACS Nano *11*, 4060–4066. https://doi.org/10.1021/acsnano.7b00725.
25. Zhou, L., Gao, M., Fu, W., Wang, Y., Luo, D., Chang, K., and Chen, M. (2020). Three-dimensional DNA tweezers serve as modular DNA intelligent machines for detection and regulation of intracellular microRNA. Sci. Adv. *6*, eabb0695. https://doi.org/10.1126/sciadv.abb0695.
26. Liu, M., Fu, J., Hejesen, C., Yang, Y., Woodbury, N.W., Gothelf, K., Liu, Y., and Yan, H. (2013). A DNA tweezer-actuated enzyme nanoreactor. Nat. Commun. *4*, 2127. https://doi.org/10.1038/ncomms3127.
27. Chen, X., Fu, X., Wu, Y., Jin, Y., and Li, W. (2020). A DNA tweezers-actuated regenerated DNAzyme nanoreactor: a fluorescence sensor for miRNA and adenosine detection. Anal. Methods *12*, 1579–1586. https://doi.org/10.1039/d0ay00142b.
28. Elbaz, J., Wang, Z.G., Orbach, R., and Willner, I. (2009). pH-stimulated concurrent mechanical activation of two DNA "tweezers". a "set-reset" logic gate system. Nano Lett. *9*, 4510–4514. https://doi.org/10.1021/nl902859m.
29. Zhu, C., Liu, D., Li, Y., Ma, S., Wang, M., and You, T. (2021). Hairpin DNA assisted dual-ratiometric electrochemical aptasensor with high reliability and anti-interference ability for simultaneous detection of aflatoxin B1 and ochratoxin A. Biosens. Bioelectron. *174*, 112654. https://doi.org/10.1016/j.bios.2020.112654.
30. Chen, R., Mao, Z., Lu, R., Wang, Z., Hou, Y., Zhu, W., Li, S., Ren, S., Han, D., Liang, J., and Gao, Z. (2022). Simple and programmed three-dimensional DNA tweezer for simultaneous one-step detection of ochratoxin A and zearalenone. Spectrochim. Acta A. *272*, 120991. https://doi.org/10.1016/j.saa.2022.120991.
31. Zhao, Y., Zhang, Y., and Jie, G. (2021). An "on-off" electrochemiluminescence biosensor based on DNA nanotweezer probe coupled with tripod capture DNA for high sensitive detection of Pb^{2+}. Sensor. Actuat. B-Chem. *326*, 128985. https://doi.org/10.1016/j.snb.2020.128985.
32. Rivetti, C., Walker, C., and Bustamante, C. (1998). Polymer chain statistics and conformational analysis of DNA molecules with bends or sections of different flexibility. J. Mol. Biol. *280*, 41–59. https://doi.org/10.1006/jmbi.1998.1830.
33. Zhang, D.Y., and Winfree, E. (2009). Control of DNA strand displacement kinetics using toehold exchange. J. Am. Chem. Soc. *131*, 17303–17314. https://doi.org/10.1021/ja906987s.
34. Grozema, F.C., Tonzani, S., Berlin, Y.A., Schatz, G.C., Siebbeles, L.D.A., and Ratner, M.A. (2009). Effect of GC base pairs on charge transfer through DNA hairpins: the importance of electrostatic interactions. J. Am. Chem. Soc. *131*, 14204–14205. https://doi.org/10.1021/ja906863k.
35. Zeraati, M., Langley, D.B., Schofield, P., Moye, A.L., Rouet, R., Hughes, W.E., Bryan, T.M., Dinger, M.E., and Christ, D. (2018). I-motif DNA structures are formed in the nuclei of human cells. Nat. Chem. *10*, 631–637. https://doi.org/10.1038/s41557-018-0046-3.
36. Zhang, P., Li, Z., Wang, H., Zhuo, Y., Yuan, R., and Chai, Y. (2017). DNA nanomachine-based regenerated sensing platform: a novel electrochemiluminescence resonance energy transfer strategy for ultra-high sensitive detection of microRNA from cancer cells. Nanoscale *9*, 2310–2316. https://doi.org/10.1039/c6nr08631d.
37. Jin, Y., Wang, J., Wu, Y., Fu, X., and Li, W. (2019). A smart DNA tweezer for universal proximity assay and logic building. Sensor. Actuat. B-Chem. *298*, 126847. https://doi.org/10.1016/j.snb.2019.126847.
38. Li, J., Chan, M.C., Yu, Y., Bei, Y., Chen, P., Zhou, Q., Cheng, L., Chen, L., Ziegler, O., Rowe, G.C., et al. (2017). miR-29b contributes to multiple types of muscle atrophy. Nat. Commun. *8*, 15201. https://doi.org/10.1038/ncomms15201.
39. Chou, J., Lin, J.H., Brenot, A., Kim, J.W., Provot, S., and Werb, Z. (2013). GATA3 suppresses metastasis and modulates the tumour microenvironment by regulating microRNA-29b expression. Nat. Cell Biol. *15*, 201–213. https://doi.org/10.1038/ncb2672.
40. Takayama, K.i., Misawa, A., Suzuki, T., Takagi, K., Hayashizaki, Y., Fujimura, T., Homma, Y., Takahashi, S., Urano, T., and Inoue, S. (2015). TET2 repression by androgen hormone regulates global hydroxymethylation status and prostate cancer progression. Nat. Commun. *6*, 8219. https://doi.org/10.1038/ncomms9219.
41. Chen, Y., and Wang, X. (2020). miRDB: an online database for prediction of functional microRNA targets. Nucleic Acids Res. *48*, D127–D131. https://doi.org/10.1093/nar/gkz757.
42. Shin, S.Y., Lee, I.H., Kim, D., and Zhang, B.T. (2005). Multiobjective evolutionary optimization of DNA sequences for reliable DNA computing. IEEE Trans. Evol. Comput. *9*, 143–158. https://doi.org/10.1109/TEVC.2005.844166.
43. Zhu, D., Huang, Z., Liao, S., Zhou, C., Yan, S., and Chen, G. (2023). Improved bare bones particle swarm optimization for DNA sequence design. IEEE T. Nanobiosci. *22*, 603–613. https://doi.org/10.1109/TNB.2022.3220795.

STAR★METHODS

KEY RESOURCES TABLE

REAGENT or RESOURCE	SOURCE	IDENTIFIER
Chemicals, peptides, and recombinant proteins		
Ammonium persulfate	Sinopharm Chemical Reagent Co., Ltd., China	Cat#: 10002618
Sodium hydroxide	Sinopharm Chemical Reagent Co., Ltd., China	Cat#: 10019762
Formamide	Sinopharm Chemical Reagent Co., Ltd., China	Cat#: 30091218
Magnesium acetate tetrahydrate	Sinopharm Chemical Reagent Co., Ltd., China	Cat#: 30110518
N,N,N′,N′-Tetramethylethylenediamine	Sinopharm Chemical Reagent Co., Ltd., China	Cat#: 80125336
Glacial acetic acid	Sinopharm Chemical Reagent Co., Ltd., China	Cat#: 10000208
Ethylenediamine tetraacetic acid disodium salt dihydrate	Sigma-Aldrich, Germany	Cat#: E5134
Tris	Sangon Biotech (Shanghai) Co., Ltd., China	Cat#: A610195
Stains-All	Sangon Biotech (Shanghai) Co., Ltd., China	Cat#: A606359
Water-DEPC Treated Water	Sangon Biotech (Shanghai) Co., Ltd., China	Cat#: B501005
Acrylamide	Sangon Biotech (Shanghai) Co., Ltd., China	Cat#: A501033
Bis-acrylamide	Sangon Biotech (Shanghai) Co., Ltd., China	Cat#: A100172
Deposited data		
miRNA sequences	Chen et al.[41]	https://mirdb.org/
Statistics FLUOR	Mendeley Data	https://doi.org/10.17632/f9w84zr3ng.1
Oligonucleotides		
See Tables S1–S7 for oligonucleotides and RNA sequences	Sangon Biotech (Shanghai) Co., Ltd., China	N/A
Software and algorithms		
Origin 2017	OriginLab (Northampton, Massachusetts, USA.)	https://www.originlab.com/index.aspx?go=PRODUCTS/Origin
Other		
NanoDrop 2000 spectrophotometer	ThermoFisher Scientific Inc., USA	Cat#: ND-2000
C1000 Touch™ Thermal Cycler with 96-Well Fast Reaction Module	Bio-Rad Inc., USA	Cat#: 1851196
DYCZ-24DN Mini Dual Vertical Electrophoresis Instrument	Beijing Liuyi Biotechnology Co., Ltd., China	Cat#: 121-2446
Tecan Spark	Tecan Trading AG, Switzerland	Cat#: 30086376

RESOURCE AVAILABILITY

Lead contact

Further information and inquiries should be directed to and will be fulfilled by the lead contact, Qiang Zhang (zhangq@dlut.edu.cn).

Materials availability

This study did not generate new unique reagents.

Data and code availability

- This paper analyzes existing, publicly available miRNA sequence data. The website for the datasets is listed in the key resources table. All the fluorescence statistics data have been deposited at Mendeley Data and are publicly available as of the date of publication. The DOI is listed in the key resources table.
- This paper does not report original code.
- Any additional information required to reanalyze the data reported in this paper is available from the lead contact upon request.

METHOD DETAILS

Reagent preparation

Four reagents need to be prepared in advance during the experimental process outlined in this article.

(1) 500 mL 10×TAE-Mg^{2+} buffer:
- Weigh Tris (24.2 g), Glacial acetic acid (5.71 mL), Ethylenediamine tetraacetic acid disodium salt dihydrate (EDTA $Na_2.2H_2O$) (1.8612 g), and Magnesium acetate tetrahydrate (13.375 g).
- Dissolve EDTA $Na_2.2H_2O$ in 10 mL of water and adjust the pH to 8.0.
- Dissolve the remaining three reagents in 400 mL of water. Heat the mixture in a 37°C water bath and continuously stir with a glass rod until completely dissolved.
- Add the remaining EDTA $Na_2.2H_2O$ solution to the mixture.
- Add water to make up the volume to 500 mL, stir evenly for later use, and store at room temperature.

This reagent is intended for dissolving DNA after dilution. For the dissolution of miRNA, ordinary pure water should be replaced with 0.1% DEPC water.

(2) 50 mL 10% APS:
- Weigh 5 g of Ammonium persulfate and dissolve it in 50 mL of water. Once completely dissolved, store it in a refrigerator at 4°C.

(3) 500 mL 40% PAGE:
- Weigh 190 g of Acrylamide and 10 g of Bis-acrylamide, dissolve them in 300 mL of water, heat the mixture in a 37°C water bath until fully dissolved.
- Add water to reach a total volume of 500 mL, shake thoroughly, and store the solution in a refrigerator at 4°C.

(4) 500 mL Stains All:
- Weigh 0.05 g of Stains All, dissolve it in 225 mL of Formamide, add 275 mL of water, shake well, and let it stand overnight in the dark. Store at room temperature.

Design of oligonucleotide sequences

All the DNA and miRNA sequences used in this article are listed in Tables S1–S7, and the experimental and modification methods for sequence application are indicated in the captions. The DNA sequences were designed by ourselves, and the miRNA sequences were derived from the Library miRDB.[41] Store DNA dry powder at −20°C, dissolve it, and store at 4°C within a week. Store miRNA dry powder at −80°C and prepare it fresh when in use. The environment for biochemical reactions is 1×TAE-Mg^{2+}, 20°C.

Annealing process protocol

The BDT used throughout the article includes three conformations (C_1, C_2, C_3), all annealed in the same manner, as illustrated in Figure S1. Specifically, place the configured sequence in the polymerase chain reaction (PCR) C1000 Touch thermal cycler and follow these steps.

- Heat to 90°C and maintain for 5 min.
- Lower to 88°C and maintain for an additional 5 min.
- Then, decrease the temperature by 0.8°C per minute until reaching 20°C.

Polyacrylamide gel electrophoresis protocol

The DNA samples were subjected to a 9% concentration polyacrylamide gel using a voltage of 100 V, and electrophoresis occurred over 80 min in 1×TAE-Mg^{2+} running buffer. Stain the electrophoresis gel for a minimum of 30 min before observation.

10 mL 9% polyacrylamide gel formation:

- Take 2.25 mL of 40% PAGE, 6.64 mL of water, 1 mL of 10×TAE-Mg^{2+}, 0.1 mL of 10% APS, and 0.01 mL of N,N,N′,N′-Tetramethylethylenediamine separately. Place them in a beaker and stir evenly.
- Inject the mixture into two intensified electrophoresis glass plates, ensuring a uniform distribution, and wait for about 30 min until the gel is fully solidified.

The concentration of BDT in each lane is typically 1×, representing 1 μM. The concentrations of each component in different lanes refer to the corresponding captions, with a volume of 20 μL added to each lane. Unless otherwise specified, we define the amount of the substance's reference as 20 pmol. The gradient experiment involves corresponding changes in the amount of the reference substance.

Fluorescence scan protocol

FAM was used for fluorescence labeling in this article, quenched with BHQ1. Set the Tecan Spark temperature to 20°C, use a 494 nm excitation wavelength, and observe the emission wavelength at 518 nm. Scan every 2 min. Fluorescence scanning is also based on 20 pmol, with the concentration and volume corresponding to the electrophoresis experiment above, unless specified otherwise.

QUANTIFICATION AND STATISTICAL ANALYSIS

Oligonucleotide information statistics

We have calculated their respective base lengths and GC content in Tables S1–S7, placing them in the last two columns of the table.

- Length: Simply count the total number of bases.
- GC content: Simply calculate the proportion of guanine and cytosine in the length using the following equation,

$$\text{GC content} = \frac{\text{Num(G)+Num(C)}}{\text{Length}}$$

Num(G) is the number of guanine, and Num(C) is the number of cytosine.

Fluorescence data statistics

In processing fluorescence data, we utilized Origin 2017 software for analysis, primarily creating line charts, bar charts, and conducting linear regression analysis.

Each fluorescence experiment was conducted three or more times using different test tubes, and the average value was calculated and included in the statistical analysis. Due to the utilization of DNA sequences from different batches, there are inherent variations in the directly measured fluorescence values. Therefore, the measurement results are normalized. In experiments not requiring multiple control groups (Figures 2A, 6B and S2), we incorporate error bars into the curve to ensure accuracy. For experiments requiring comparison, we employ the dotted line method for clarity, preventing visual confusion arising from an excess of error bars. Fluorescence statistical data is available in key resources table "Statistics FLUOR".

This article uses two normalization methods,

- F/F_0: F_0 represents the initial fluorescence value, and F denotes the specific fluorescence value at each moment. Therefore, F/F_0 indicates the proportional relationship between fluorescence at each moment and the initial value. This coordinate system facilitates a straightforward observation of the amplitude of fluorescence change relative to the initial value.
- $\Delta F/\Delta F_{Max}$: ΔF denotes the increment of the current fluorescence value relative to the lowest fluorescence value, and ΔF_{Max} represents the maximum ΔF in the entire reaction. Consequently, this system aids in clearly observing the growth amplitude of the V-shaped fluorescence before and after the lowest point in our scheme.

Both methods are advantageous in mitigating these experimental biases.